Supplementary Information for

Robustness of Trion State in Gated Monolayer MoSe₂ under Pressure

Zeya Li[1,2†], Feng Qin[1,2†], Chin Shen Ong[3†], Junwei Huang[1,2†], Zian Xu[4], Peng Chen[1,2], Caiyu Qiu[1,2],

Xi Zhang[1,5], Caorong Zhang[1,5], Xiuxiu Zhang[4], Olle Eriksson[3,6],

Angel Rubio[7,8,9]*, Peizhe Tang[4,7]*, Hongtao Yuan[1,2]*

[1] *National Laboratory of Solid State Microstructures, and Collaborative Innovation Center of Advanced Microstructures, Nanjing University, Nanjing 210093, China.*

[2] *College of Engineering and Applied Sciences, and Jiangsu Key Laboratory of Artificial Functional Materials, Nanjing University, Nanjing 210023, China.*

[3] *Department of Physics and Astronomy, Uppsala University, Uppsala 75120, Sweden.*

[4] *School of Materials Science and Engineering, Beihang University, Beijing 100191, China.*

[5] *School of Physics, Nanjing University, Nanjing 210000, China.*

[6] *School of Science and Technology, Örebro University, Örebro 70182, Sweden.*

[7] *Max Planck Institute for the Structure and Dynamics of Matter, Center for Free Electron Laser Science, Hamburg 22761, Germany.*

[8] *Center for Computational Quantum Physics, Simons Foundation, Flatiron Institute, New York 10010, USA.*

[9] *Nano-Bio Spectroscopy Group, University of the Basque Country (UPV/EHU), San Sebastián 20018, Spain.*

CONTENTS

*Angel Rubio: angel.rubio@mpsd.mpg.de

*Peizhe Tang: peizhet@buaa.edu.cn

*Hongtao Yuan: htyuan@nju.edu.cn

I. Details of device fabrication, DFT calculation and QMC simulations

<u>Device fabrication and photoluminescence measurements.</u> Monolayer $MoSe_2$ and atomically-thin *h*-BN flakes were cleaved from their bulk crystals onto polydimethylsiloxane (PDMS) surfaces by mechanical exfoliation and then successively transferred onto a 300-μm-diameter diamond culet with prepatterned Ti/Au electrodes, forming an *h*-BN/$MoSe_2$/*h*-BN sandwiched structure. The prepatterned electrodes (Ti/Au, 5/15 nm) were evaporated with a shadow mask. The thickness of monolayer $MoSe_2$ is identified by the optical image and PL spectrum. The whole process of sample preparation was completed in ambient atmosphere. The Pt electrodes with a thickness of 4 μm were then placed at the edge of the Ti/Au electrodes on the diamond culet to ensure good electrical contact under high pressure. Silicon oil was used as the transmitting pressure medium to provide a hydrostatic pressure. The absolute value of the applied pressure was calibrated by the peak position of ruby fluorescence at room temperature [1]. The PL measurements were performed using a confocal Raman system (WITec Alpha 300) with a laser wavelength of 532 nm. The laser power was set as 1 mW to avoid sample heating for both room-temperature and low-temperature PL measurements. The laser beam was focused on the sample with a long working distance ×50 objective lens. Low-temperature PL measurements were performed with DAC installed in a microscopy cryostat. The gate bias was applied by a Keithley 2400. After all the low-temperature measurements were performed, the sample was warmed to room temperature to apply a higher pressure through DAC. All the PL spectra were fitted by multiple Voigt functions to clarify the peak energies, linewidths and integrated PL peak intensities.

<u>Density functional theory calculations.</u> The DFT calculations were performed with the Vienna *ab initio* simulation package (VASP) [2] using the projector augmented wave method (PAW) [3, 4]. The plane-wave energy cutoff was 550 eV, and the convergence criteria of the forces was set as 10^{-3} eV/Å. The Brillouin zones were sampled by $15 \times 15 \times 4$ and $15 \times 15 \times 1$ Monkhorst-Pack grids for the bulk structures and the slab models, respectively. The exchange-correlation functional was chosen as the Perdew–Burke–Ernzerhof (PBE)-type generalized gradient approximation (GGA) [5]. The van der Waals correction [6, 7] was considered within the calculations. Moreover, spin-orbit coupling was included in the electronic structure calculations. The lattice constants *a* (and *b*) and *c* of the $MoSe_2$ bulk structure were 3.332 Å and 13.17 Å, respectively, after full relaxation, which were consistent with previous studies [8, 9]. The influence of hydrostatic pressures was simulated by the application of geometric optimization on the $MoSe_2$ bulk structure under zero pressure, where a similar method was employed in a previous study [10]. After that, monolayer $MoSe_2$ models were built directly for further calculations, where a vacuum layer of 20 Å was added in the vertical direction of each slab structure.

The calculations with the GGA-PBE functional underestimated the bandgap at the K (and K′) points for monolayer $MoSe_2$ while correctly describing the evolution of the Λ–K crossover of the conduction band with increasing pressure. Thus, we used the HSE06 hybrid functional [11, 12] to correct the band gap of monolayer $MoSe_2$. Under zero pressure, the calculated result was 1.99 eV for the direct band gap at the K point, which was very close to that from G_0W_0 calculations [13] (2.08 eV). However, the HSE06 functional failed to describe the Λ–K crossover of conduction bands with increasing pressure. In our QMC simulations, we used the direct bandgap from the HSE06 functional for the monolayer under zero pressure (1.99 eV), while the change in bandgap with respect to

77 increasing pressure (28 meV/GPa) and the effective masses were obtained by using the GGA-PBE
78 functional.

79 <u>Quantum Monte Carlo simulations for excitons and trions.</u> To calculate the binding energies of the
80 exciton (trion), we employ an effective-mass model for two (three) charged point-like particles in
81 2D. Each particle is assumed to have a parabolic band of effective mass m_i^*. By separating out the
82 center-of-mass motion [14-16], we recast the internal two-body dynamics of the excitons in terms of
83 their relative coordinates using a one-particle ($i = 1$) effective-mass Hamiltonian, which has the form

$$H_{\text{exciton}} = -\frac{\hbar^2}{2\mu}\Delta + V_{2\text{D}}(\rho), \tag{1}$$

84

85 and the internal three-body dynamics of the trion using a two-particle ($i = 1, 2$) effective-mass
86 Hamiltonian, which has the form

$$H_{\text{trion}} = -\frac{\hbar^2}{2\mu}\Delta_1 - \frac{\hbar^2}{2\mu}\Delta_2 - \frac{\hbar^2}{M}\boldsymbol{\nabla}_1 \cdot \boldsymbol{\nabla}_2$$
$$+ V_{2\text{D}}(\rho_1) + V_{2\text{D}}(\rho_2) - V_{2\text{D}}(|\boldsymbol{\rho}_1 - \boldsymbol{\rho}_2|), \tag{2}$$

87

88 where $\mu = \frac{1}{m_e^{-1} + m_h^{-1}}$ is the reduced effective mass of the electron-hole pair, $M = 2\, m_e + m_h$ is the
89 total mass of trion, Δ_i and $\boldsymbol{\nabla}_i$ are, respectively, the Laplacian and gradient operators acting on
90 functions of $\boldsymbol{\rho}_i$. For excitons, the i label is implicit (see Fig. 4c). For trions, relative coordinates, $\boldsymbol{\rho}_i$,
91 are defined as the spatial relative vectors between identical charges ($i = 1, 2$) and nonidentical
92 charges (see Fig. 4d). For the trion, the hole has the nonidentical charge, while the electrons have
93 identical charges. $V_{2\text{D}}$ is the effective screened Coulomb potential energy of the Rytova-Keldysh
94 form [17-20],

$$V_{2\text{D}}(\rho) = -\frac{\pi e^2}{2\rho_0 \epsilon^*}\left[H_0\left(\frac{\rho}{\rho_0}\right) - Y_0\left(\frac{\rho}{\rho_0}\right)\right], \tag{3}$$

95

96 where H_0 and Y_0 are, respectively, the Struve and Bessel functions of the second kind, e is the
97 (positive) elementary charge, ϵ^* is the effective dielectric constant that is the average of the dielectric
98 constants of the media above (ϵ_{above}) and below (ϵ_{below}) the 2D monolayer and ρ_0 is the effective
99 screening radius. Since ρ_0 is related to the finite thickness of the 2D monolayer, d, and its in-plane
100 dielectric constant, $\epsilon_{2\text{D}}$, by $\rho_0 = \frac{d\epsilon_{2\text{D}}}{\epsilon_{\text{above}} + \epsilon_{\text{below}}}$, setting ρ_0 to 4 times the Bohr radius of hydrogen is
101 equivalent to setting $\epsilon_{2\text{D}}$ to 3.11 if we approximate the thickness of the 2D monolayer to 8.3 Å. The
102 third term on the RHS of Eq. (2) that is $\propto \boldsymbol{\nabla}_1 \cdot \boldsymbol{\nabla}_2$ is the mass-polarization term, also known as the
103 Hughes–Eckart term [21]. If we were to compare Eq. (2) with the Hamiltonian for the H$^-$ ion, the
104 Hughes–Eckart term corrects for the finite mass, M, of the nonidentical charge within the effective-
105 mass approximation. In these effective Hamiltonians, we use effective masses obtained from DFT at
106 different pressures. For the bandgap at the K point in monolayer MoSe$_2$ under no pressure, we used
107 the HSE06 hybrid functional to correct the bandgap.

108 We use the variational QMC to obtain the wavefunction and eigenvalues of excitons and trions. Our
109 QMC calculations use 500 random walkers and step lengths that give an acceptance ratio of 0.5. Each
110 walker makes a total of 2.0×10^5 Monte Carlo moves and 5000 thermalization steps. Next, we define
111 our trial exciton and trion wavefunctions. For the exciton, energy minimization is carried out using
112 the 2D hydrogenic $1s$ state as the trial wavefunction, $\phi_{\text{exciton}}^{1s}(\rho) = A \exp(-2\alpha\rho)$, where A is a
113 normalization constant and α is the variational parameter; for the trion, the product of the $1s$ exciton
114 wavefunction is used as the trial wavefunction, $\phi_{\text{trion}}^{1s}(\boldsymbol{\rho}_1, \boldsymbol{\rho}_2) = B \exp(-2\alpha\boldsymbol{\rho}_1)\exp(-2\alpha\boldsymbol{\rho}_2)$,
115 where B is a normalization constant and $\boldsymbol{\rho}_i$ is the electron–hole relative coordinates. The latter
116 wavefunction is reminiscent of the 1^1S ground state of H^- and He, which is spin anti-symmetric and
117 has the orbital character of $1s^2$ (or $1s \otimes 1s$). In this choice of this trial wavefunction, there is no
118 correlation between $\boldsymbol{\rho}_1$ and $\boldsymbol{\rho}_2$. Correlations are subsequently added via the multiplication of the
119 mass-polarization factor, $(1 + c|\boldsymbol{\rho}_1 - \boldsymbol{\rho}_2|)$, to the abovementioned $\phi_{\text{trion}}(\boldsymbol{\rho}_1, \boldsymbol{\rho}_2)$.

120 The effective screened Coulomb interaction inside the 2D monolayer is calculated using the Rytova–
121 Keldysh model [17, 18], wherein the experimental h-BN dielectric constant [22] of 6.07 is used as
122 the dielectric constant of the media above (ϵ_{above}) and below (ϵ_{below}) the 2D monolayer. In the
123 Rytova–Keldysh model, the effective screening radius, ρ_0, defines the length scale at which the
124 Coulomb potential, $V(\rho)$, crosses over from being 2D-like at a short range (for $\rho < \rho_0$), to being 3D-
125 like at a long range (for $\rho > \rho_0$). In this work, we use ρ_0 as our only fitting parameter, setting it to ρ_0
126 = 2.1 Å, which is 4 times the Bohr radius of hydrogen, to fit the calculated E_b^{exciton} at 0.22 GPa.
127 Without further fitting other parameters, we calculate E_b^{exciton} for the remaining pressure range and
128 E_b^{trion} at all pressures. Note that in our work we defined the trion binding energy as E_b^{trion}, i.e.,
129 $E_b^{\text{trion}} = E_{\text{exciton}} - E_{\text{trion}}$ following a long practice used in the field of low-dimensional
130 semiconductors [23, 24]. The trion state is regarded as a bound state of an exciton and an electron
131 and thus the "trion binding energy" is regarded as the energy difference of the exciton and trion state.
132 In our calculations, we considered the increase of the bandgap as pressure increases and observed the
133 related increase in exciton binding energy due to the enlargement of the effective masses of electrons
134 and holes. But the energy variation of exciton peak is smaller than the change of bandgap (see Fig. 4
135 in the main text). Such an observation is analogous to the *cancellation effect* reported previously [25-
136 28], in which the increase in bandgap is partly compensated by the increase in exciton binding energy
137 and thus the absolute energy level of the exciton remains relatively constant. In our calculations, the
138 observed compensation is smaller than that obtained by varying dielectric environments, as our
139 model does not consider the decrease in dielectric screening (which will increase the exciton binding
140 energy) as the bandgap increases as pressure increases [25].

141

II. Fabrication of hBN-gated monolayer MoSe₂ devices in a DAC cell

We selected $MoSe_2$ as an example for studying excitonic physics under pressure based on the results of comparing the photoluminescence (PL) properties of four commonly-used monolayer transition metal dichalcogenides (TMDCs), including MoS_2, $MoSe_2$, WS_2, and WSe_2. For the PL spectra of monolayer MoS_2 and $MoSe_2$ on the diamond culet (Supplementary Fig. 1a), it is evident that the PL emission peak of $MoSe_2$ has both stronger intensity and narrower linewidth than those of MoS_2, suggesting a higher quantum yield of $MoSe_2$. We did not use WS_2 and WSe_2 due to the complexity in their excitonic states reflected by their low-temperature PL emissions. Therefore, we chose monolayer $MoSe_2$ as the target material for probing and studying excitonic states under pressure via our *gating-under-pressure* technique.

To investigate the excitonic physics of $MoSe_2$ under pressure, we fabricated a monolayer $MoSe_2$ device using h-BN as a dielectric material for the back gate in the diamond anvil cell (DAC) setup. There are three main steps in the fabrication process of our device, as illustrated in Supplementary Fig. 1b–d.

Step 1: MoSe₂ on PDMS. The monolayer $MoSe_2$ was mechanically exfoliated onto PDMS (polydimethylsiloxane) and then selected via its optical contrast (Supplementary Fig. 1b) and PL spectrum. Thin h-BN flakes were chosen according to their optical contrast only. **Step 2: MoSe₂/h-BN on diamond.** In the dry transfer process, the h-BN thin flake was transferred onto a 300-μm-diameter diamond culet with prepatterned electrodes, partially covering the right electrode and not physically contacting the left electrode. The distance between the prepatterned Ti/Au electrodes was approximately 20 μm, and the thickness of Ti/Au was 5/15 nm. Subsequently, the monolayer $MoSe_2$ (connected with a thick $MoSe_2$ flake) was transferred on top of the thin h-BN flake and isolated to the right electrode with h-BN as the dielectric layer, forming a vertical $MoSe_2$/h-BN/Au sandwiched structure (Supplementary Fig. 1c). Simultaneously, the thick part of this $MoSe_2$ flake was electrically contacted to the left electrode, which served as the source electrode. **Step 3: h-BN/MoSe₂/h-BN on diamond.** Another h-BN flake was transferred to completely cover monolayer $MoSe_2$ (Supplementary Fig. 1d). This h-BN flake can protect monolayer $MoSe_2$ from degradation and effectively improve the data quality when immersed in the pressure transmitting medium. Here, we used silicon oil as the pressure transmitting medium to provide hydrostatic pressure. **Finally**, we sealed the DAC after dropping the silicon oil and connecting the electrodes to the outside of the DAC.

In each process, the PL spectrum of $MoSe_2$ (Supplementary Fig. 1e) and the corresponding PL emission energy and peak intensity of the exciton (Supplementary Fig. 1f) are obtained. On the one hand, the exciton emission energy shows a slight redshift after Step 3 (encapsulating $MoSe_2$ with h-BN), which is attributed to the reduction of both the bandgap and exciton binding energy due to the increased dielectric screening of $MoSe_2$. On the other hand, the PL intensity of the exciton peak increases after Step 3. This enhancement can be attributed to the optical interference effect in the multi-layered substrate, which was recently confirmed in monolayer WS_2 within a WS_2/h-BN/Au structure [29].
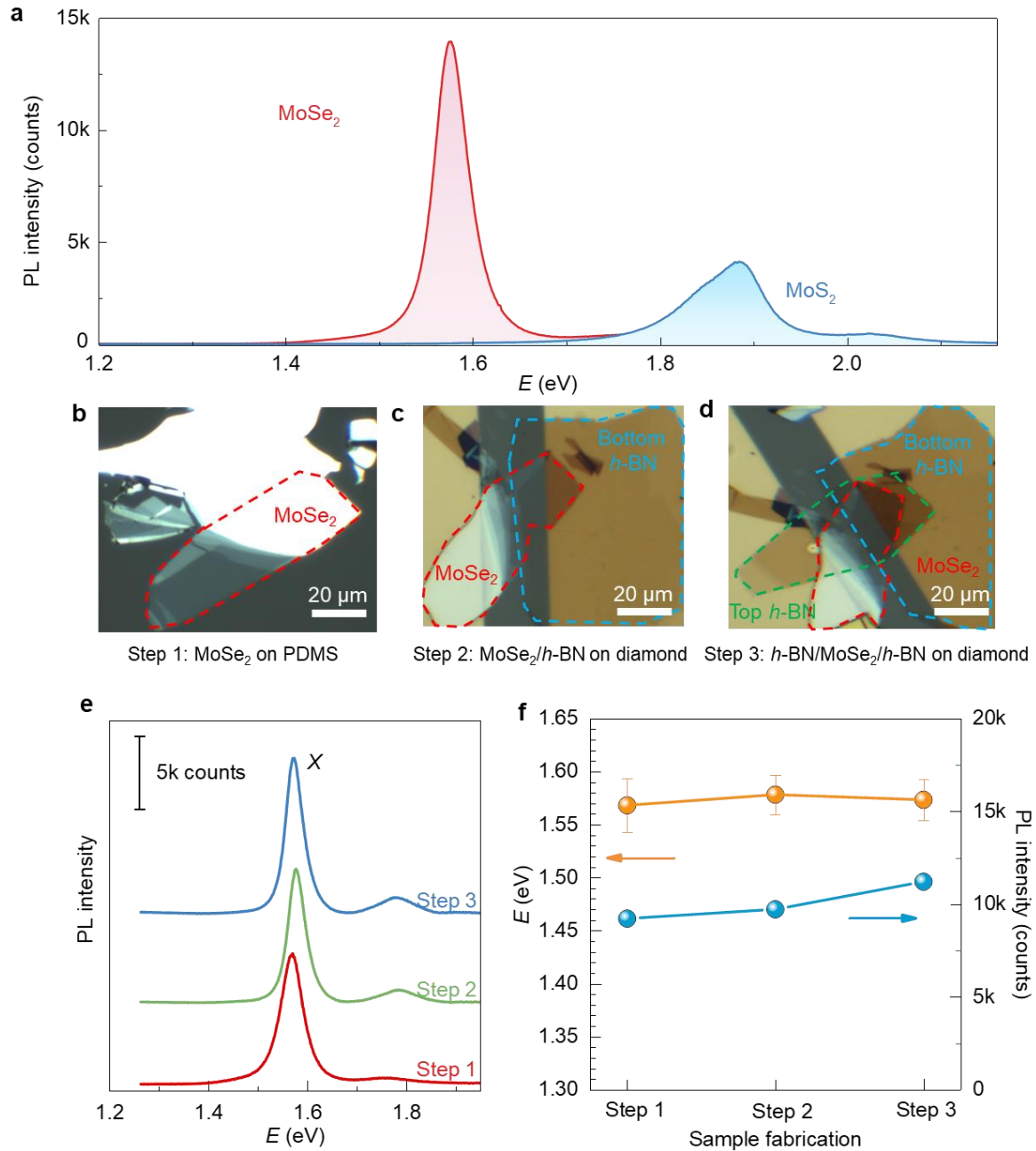
Supplementary Figure 1. Fabrication process of gated monolayer MoSe₂ device in DAC. **a**, Comparison of the PL spectra of monolayer $MoSe_2$ (red curve) and MoS_2 (blue curve) on a diamond culet. The PL measurements were performed under the same conditions (the laser power was 1 mW, and the integrated time was 20 seconds) at room temperature. **b–d**, Optical image of **b**, MoSe₂ on PDMS in step 1, **c**, h-BN/MoSe₂ heterostructure on diamond in step 2, and **d**, h-BN/MoSe₂/h-BN heterostructure on diamond in step 3. The scale bar is 20 μm. **e**, PL spectrum obtained during the process of device fabrication of **b–d**. **f**, The exciton emission energy and PL intensity evolution during the device fabrication process. The error bar is the full width at half maximum (FWHM) of the PL peak.

III. Confirmation of the effective lattice compression of monolayer TMDCs under pressure

To confirm whether the pressure inside DAC is hydrostatic, we checked the ruby PL peak at each pressure point (Supplementary Fig. 2a). Normally, the line width of the ruby peak would become broader when the pressure becomes nonhydrostatic. While in our case, the line width of our ruby peaks shows almost no change with increasing pressure up to 4.2 GPa (Supplementary Fig. 2b), indicating that the pressure can be considered hydrostatic based on the silicon oil pressure medium. More importantly, such hydrostatic pressure is rather uniform. Supplementary Fig. 2c-d shows the pressure as a function of distance from the center of DAC under a pressure of 2.5 GPa. One can see the pressure fluctuation is as small as 0.2 GPa across a distance of 50 μm.

We performed high-pressure Raman measurements on monolayer TMDCs within DAC to confirm that the pressure applied on monolayer samples is similar to those scenarios in bulk-type samples and to verify that the lattice is effectively compressed. At ambient pressure, we focus on the two unique Raman modes in monolayer MoS_2 (Supplementary Fig. 3a): the A_{1g} mode located at 404 cm^{-1} corresponding to the out-of-plane vibrations and the E_{2g}^1 mode located at 384 cm^{-1} corresponding to the in-plane vibrations [30]. Based on the fact that the compression of the lattice normally causes the stiffening of the Raman modes in MoS_2 samples [31], we confirm the applied pressure in our monolayer samples by comparing the Raman modes with two other different TMDC samples: bulk samples under hydrostatic pressure and ultrathin samples under uniaxial strain. Note that here we chose MoS_2 instead of $MoSe_2$ as our example because the signal of the in-plane vibration E_{2g}^1 mode in $MoSe_2$ is technically too weak to be detected since there is no resonance Raman effect [32] under the excitation of a 532 nm laser, and only the out-of-plane A_{1g} mode can be clearly observed. Therefore, we do not have any opportunity to study the pressure effect on the in-plane compression in monolayer $MoSe_2$ due to its undetectable in-plane E_{2g}^1 mode. Fortunately, for MoS_2 monolayers, the signals for both the E_{2g}^1 and A_{1g} modes are strong enough for a reliable comparison (Supplementary Fig. 3a).

First, for bulk MoS_2 under hydrostatic pressure, in which the applied pressure is widely accepted to be isotropic [31], both the A_{1g} and E_{2g}^1 modes of the compressed MoS_2 lattice show an obvious blueshift with increasing pressure. Such Raman blueshifts are directly associated with lattice compression in bulk MoS_2 and are reported to shift at a rate of 3.7 cm^{-1}/GPa for the A_{1g} mode and 1.8 cm^{-1}/GPa for the E_{2g}^1 mode in bulk MoS_2 [31]. The ratio between the changing rates of the A_{1g} mode and E_{2g}^1 mode with pressure in bulk MoS_2 is close to 2, which is almost the same as the value in our monolayer case (Supplementary Fig. 3b). More importantly, the linear behaviour of all the modes in our monolayer case directly indicate the absence of notable non-hydrostatic stress components [33]. Note that in Supplementary Fig. 3c, we also provide the Raman shifts of the out-of-plane vibration A_{1g} mode in monolayer $MoSe_2$ under different pressures. One can see that, similar to monolayer MoS_2, the Raman shifts of the out-of-plane vibration A_{1g} mode in monolayer $MoSe_2$ shows a linear blueshift with increasing pressure. These facts indicate that the pressure is effectively applied to our monolayer materials and that the lattice of the monolayer structure is compressed.

Second, to confirm that the pressure is along both in-plane and out-of-plane directions in our case, we compare our results under pressure with those cases under biaxial tensile strain [34] or uniaxial tensile strain (Supplementary Fig. 3d). For those cases under biaxial/uniaxial tensile strain, the sample is stretched a lot along in-plane directions, while compressed only a little along out-of-plane directions, resulting in the remarkable redshift for in-plane E_{2g}^1 mode while almost no shift for out-of-plane A_{1g} modes [35]. However, our monolayer MoS_2, with a pressure-induced compression of the in-plane lattice constant, shows a remarkable blueshift for the E_{2g}^1 mode rather than a redshift. This fact directly excludes the existence of in-plane lattice expansion in DAC.

Based on the comparisons between our results and those in the literature, we have confirmed that our

237 monolayer samples undergo a quasi-hydrostatic pressure (not the type of strictly-hydrostatic pressure
238 but indeed being the 3D compressed pressure in three dimensions).
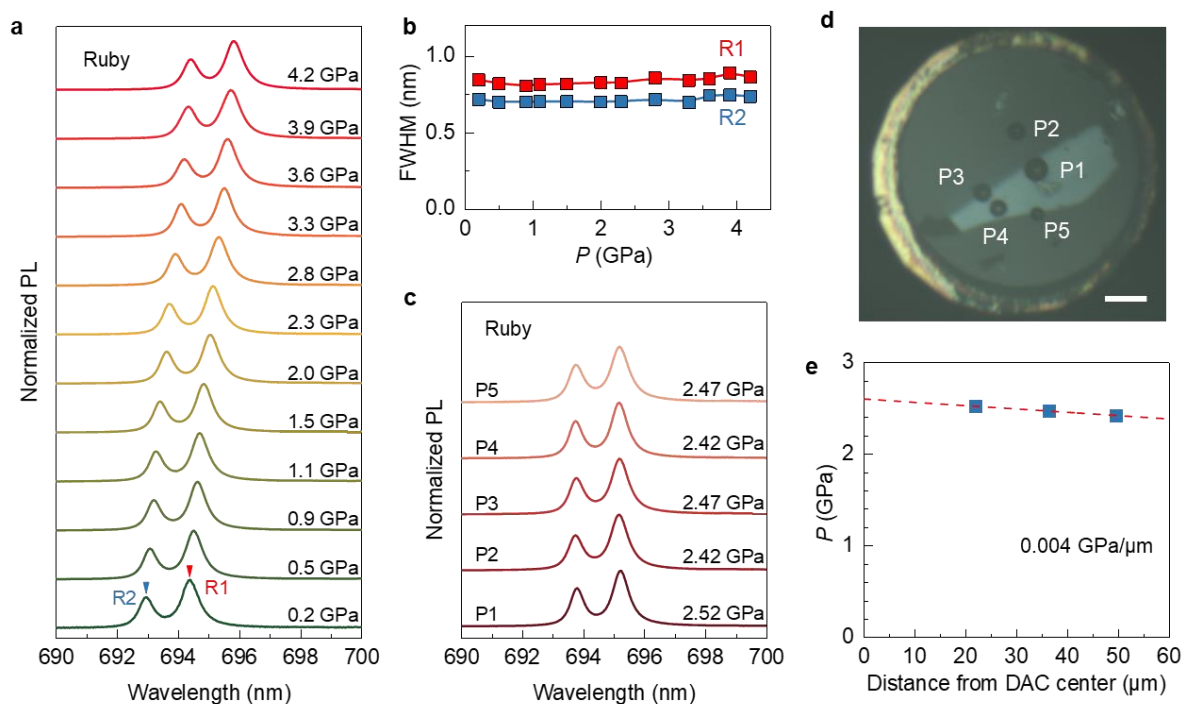
240 **Supplementary Figure 2. Ruby photoluminescence for determining pressure. a**, PL spectra of ruby under
241 different pressures for the monolayer $MoSe_2$ sample in the main text. The arrows highlight the R1 and R2 peaks.
242 **b**, The full width at half maximum (FWHM) of the R1 and R2 peaks as a function of pressure. **c**, Normalized
243 PL spectra of ruby at different positions inside the DAC at a pressure of approximately 2.5 GPa **d**, The
244 corresponding optical image of ruby distribution inside the DAC. The scale bar is 50 μm. **e**, Pressure values in
245 the DAC as a function of the distance from the DAC center for a specific case.

246
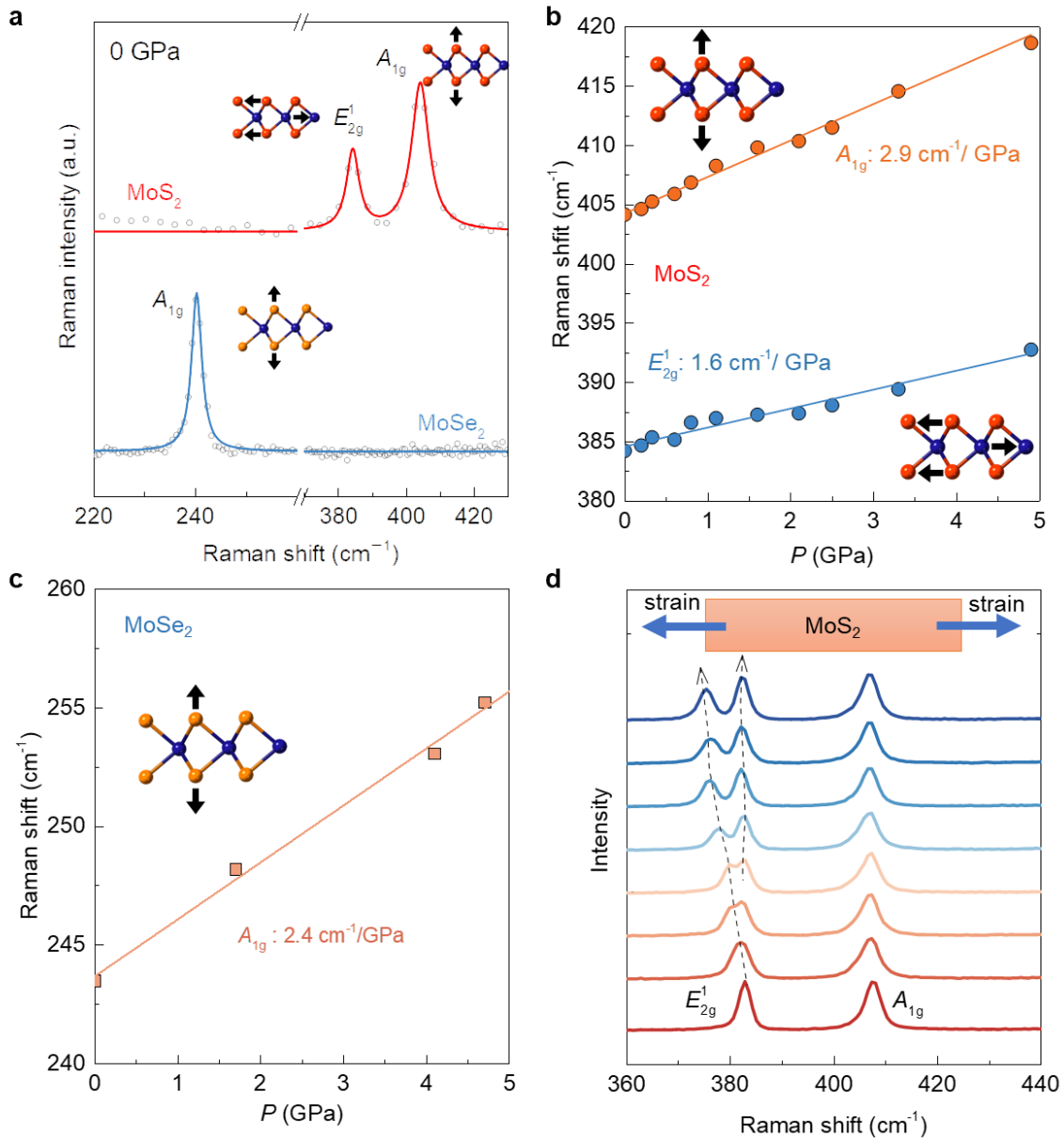
Supplementary Figure 3. Raman spectra of monolayer MoS₂ under compression (pressure) and tensile strain at room temperature. **a,** Comparison of Raman spectra of monolayer MoS₂ and MoSe₂ at ambient pressure. Inset: schematic figures of the out-of-plane A_{1g} and in-plane E_{2g}^1 vibration modes. The blue and red balls represent the Mo and S (or Se) atoms. The black arrows represent the vibration of the corresponding atom. **b,** Raman shifts of the A_{1g} (orange circles) and E_{2g}^1 (blue circles) modes as a function of pressure in monolayer MoS₂. The solid lines are linear fits. Inset: schematic figures of out-of-plane A_{1g} and in-plane E_{2g}^1 vibration modes. **c,** Raman shifts of the A_{1g} modes as a function of pressure in monolayer MoSe₂. The solid lines are linear fits. Inset: schematic figures of out-of-plane A_{1g} vibration modes. **d,** Raman spectra of few-layer MoS₂ with increasing uniaxial strain up to 2%. Inset: schematic of uniaxial strain applied on few-layer MoS₂. The E_{2g}^1 peak splits into two subpeaks as the degeneracy is lifted owing to the lattice symmetry breaking of MoS₂ under strain [36] and the central part of the two split peaks shows a clear redshift with increasing strain, while A_{1g} shows no measurable shift.

9

IV. Evidence for the Λ–K crossover and direct-to-indirect optical transition in pressurized monolayer MoSe₂

To clearly demonstrate the improved data quality with *h*-BN encapsulation, we directly compare the normalized PL spectra of MoSe₂ with and without *h*-BN encapsulation, as shown in Supplementary Fig. 4a. Only in the case of encapsulated MoSe₂ can we observe a small PL peak at higher energy than the exciton (X), which is commonly referred to as the X' exciton. These excitons are caused by the spin-split valence band at the K points due to the strong spin–orbit coupling of monolayer MoSe₂. Based on the enhanced PL intensity (Supplementary Fig. 1f) and detectable X and X' excitons at room temperature, we demonstrate that the *h*BN-encapsulated samples can serve as a better platform for studying the optical properties of TMDCs under pressure.

To determine the pressure evolution of the band structure of monolayer MoSe₂, we analyzed the PL spectra under various pressures and discussed the consequent change in excitonic states. The inset of Supplementary Fig. 4a shows the normalized PL spectra of *h*BN-encapsulated MoSe₂ under pressures ranging from 0.1 to 4.7 GPa (original data of Fig. 1c in the main text). Supplementary Fig. 4b shows the emission energy and PL intensity of the exciton peak as a function of pressure. From 0.1 to 3.0 GPa, the exciton emission energy increases linearly with increasing pressure, which is caused by the pressure-induced bandgap increasing at the K point. However, at pressures higher than 3.0 GPa, the exciton emission energy exhibits a redshift trend with increasing pressure, which may be caused by the Λ–K crossover transition with the emission process transiting from the direct to indirect optical transition, corresponding to the lowering of the conduction band minimum at the Λ point. The PL intensity decreases with increasing pressure to 3.0 GPa and becomes undetectable with further increased pressure. We deduce that such changes in exciton emission energy and peak intensity correspond to the Λ–K crossover in the band structure of monolayer MoSe₂, as mentioned in the main text.

To further verify the reproducibility of the Λ–K crossover and the resulting direct-to-indirect bandgap transition in monolayer MoSe₂, we fabricated several MoSe₂ devices with and without *h*-BN capping layers in the DAC setup and measured their room-temperature PL spectra at various pressures. Supplementary Figure 4c shows the emission energy and PL intensity of the exciton peak as a function of pressure for a MoSe₂ sample without *h*-BN encapsulation. The exciton emission energy blueshifts with pressure up to 3.0 GPa and then starts to show a redshift trend. The PL intensity decreases to a relatively low level above 3.0 GPa. These pressure-dependent behaviors are similar to those of the sample with the capping layer of *h*-BN (Supplementary Fig. 4b). We determined the critical pressure of the Λ–K crossover by using the abrupt decrease in the exciton peak intensity as a simple criterion. Supplementary Figure 4d shows the critical pressures obtained in four different monolayer MoSe₂ samples, which are similar and yield an average value of approximately 3.2 GPa.
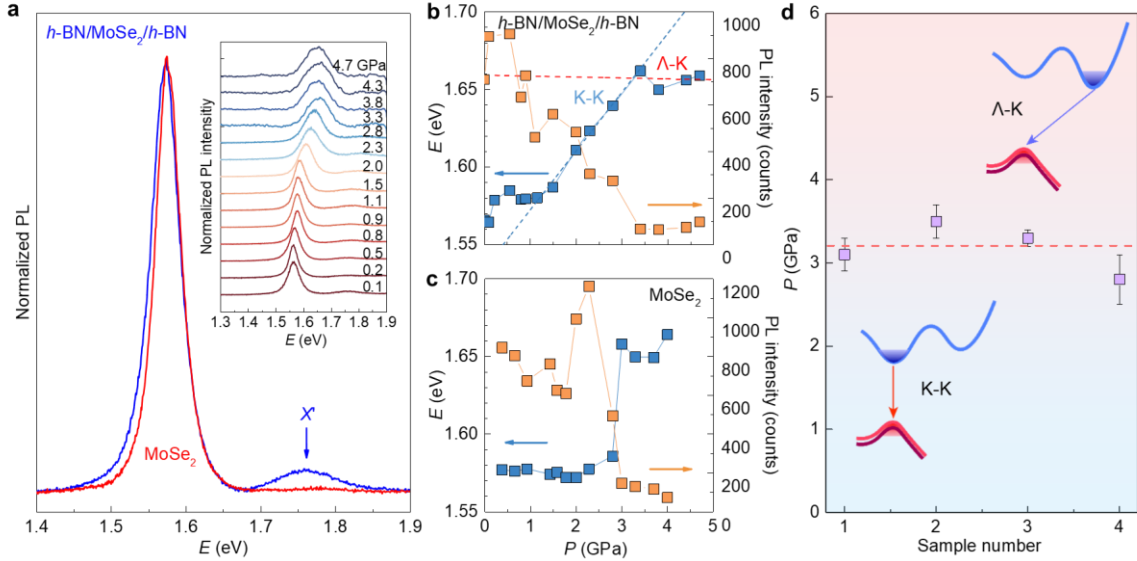
Supplementary Figure 4. Pressure-dependent PL spectra of monolayer MoSe₂. a, Comparison of room-temperature PL spectra of monolayer MoSe₂ with and without *h*-BN encapsulation in DAC. The blue arrow points to the peak corresponding to the *X'* exciton. Inset: Room-temperature PL spectra of monolayer MoSe₂ with an *h*-BN capping layer under pressure from 0.1 GPa to 4.7 GPa. The PL spectra are normalized to the maximum PL intensity and shifted on the Y-axis for better visualization. **b**, Exciton emission energy (blue square) and PL intensity (orange square) as a function of pressure with *h*-BN capping layers. **c**, Emission energy (blue square) and PL intensity (orange square) of exciton as a function of pressure of MoSe₂ without an *h*-BN capping layer. **d**, Critical pressure of the Λ–K crossover in four individual monolayer MoSe₂. The error bar represents the uncertainty of the critical pressure. The horizontal dashed line highlights the critical pressure of 3.2 GPa. Inset: schematic illustration of the K–K direct transition (bottom) and Λ–K indirect transition (top).

Supplementary Figure 5 presents the spatial distribution of the exciton peak intensity at various pressures, demonstrating three important features: i) the homogeneity of the applied pressure in the sample, ii) the details of the pressure distribution of the sample during compression, and iii) a more intuitive process of pressure-induced Λ–K crossover in MoSe₂. On the one hand, the PL intensities in the sample are rather uniform across a wide range of pressures, implying that the entire sample undergoes a uniform external pressure field in the compression process. On the other hand, the PL intensities of the exciton peak drop rapidly with pressure and approach the background level at 3.3 GPa. As discussed above, this quenching of PL with increasing pressure corresponds to the Λ–K crossover and the direct-to-indirect bandgap transition therein.

Interestingly, at 0 GPa, one can see several fine lines in the PL intensity mapping across the sample (denoted as the "line-shaped area"), in which the PL intensity is slightly smaller than the values in "normal area". However, the several fine lines across the sample become clearer under pressure and the PL intensity of these "line-shaped area" becomes larger than the "normal area". To figure out the origin of such PL intensity reversal between these "line-shaped area" and "normal area", we compare the corresponding PL spectra at the "line-shaped area" and the "normal area" (Supplementary Fig. 6). One can see at 0 GPa the PL peak energy is smaller at the "line-shaped area" compared to the "normal area" (Supplementary Fig. 6a), indicating that the sample therein is under a small tensile strain. Such a strain might increase the non-radiation recombination of excitons and decrease the PL intensity. While, once we applied an external pressure (Supplementary Fig. 6b), the evolution of the

exciton energy with the applied pressure in the "line-shaped area" and "normal area" can be different and the MoSe$_2$ in these two areas shows different sensitivities to the pressure due to the residual lattice strain in the "line-shaped area" (Supplementary Fig. 6c). Thus, the PL peak intensity in the "line-shaped area" decreases slower with pressure than that in the "normal area" (Supplementary Fig. 6d) and shows the PL intensity inverse, which can be verified by an intensity crossover at about 0.3 GPa (Supplementary Fig. 6e). Since the residual strain in transferred vdW samples is common and can be easily controlled, we believe that such non-uniformity in PL mapping can be avoided by annealing the initial sample or optimizing the sample transfer procedure.
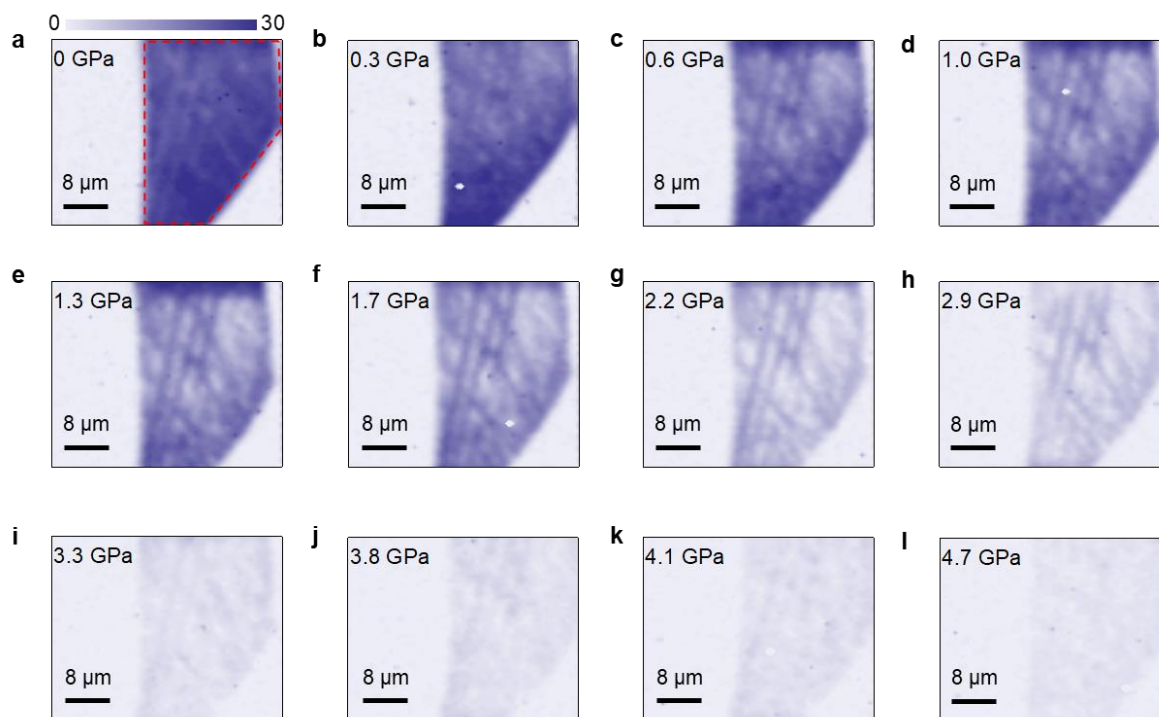
Supplementary Figure 5. PL mapping of the integrated intensity of the *X* peak in pressurized MoSe$_2$ at different pressures. a–l, Images are obtained at a fixed temperature of 300 K with different pressures. The scale bar is 8 μm. The color bar indicates the exciton peak integrated intensity. The red dashed line highlights the region of monolayer MoSe$_2$. Note that data at 0, 1.3, 2.2, and 3.3 GPa have already been given in Fig. 1e in the main text.
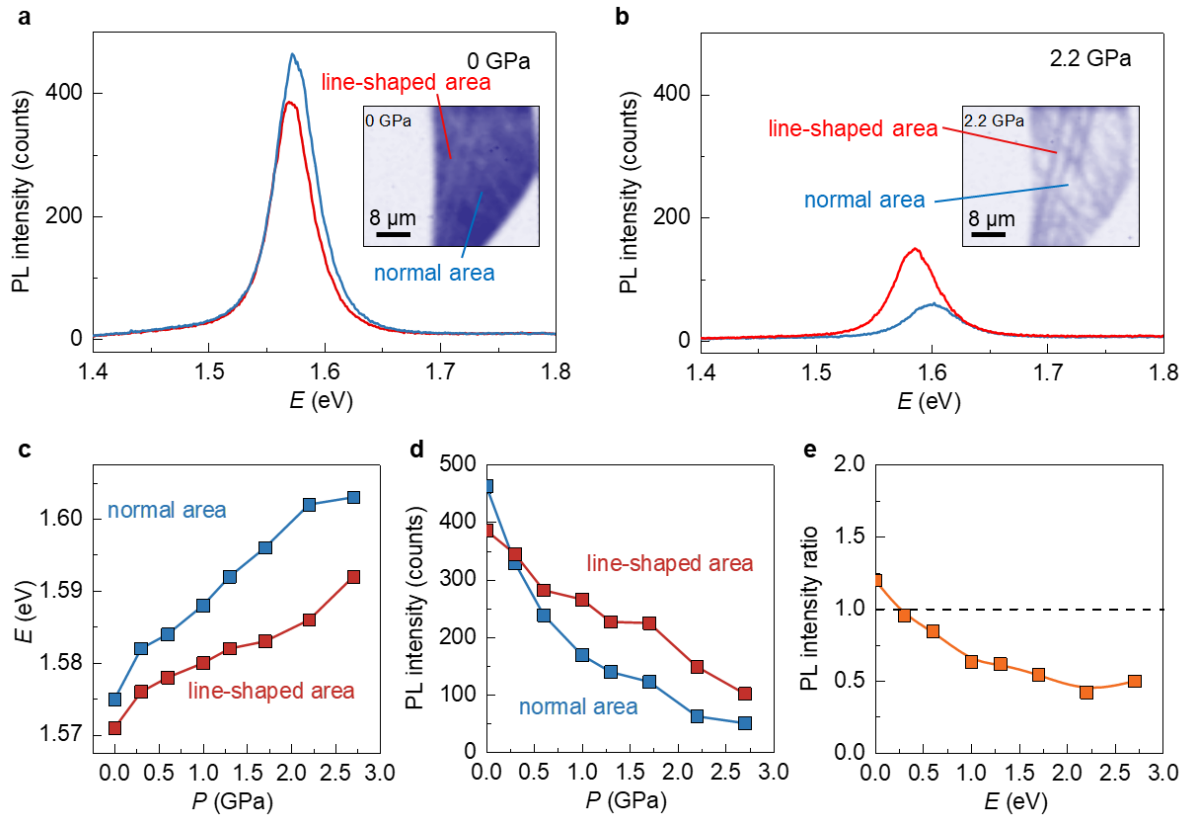
Supplementary Figure 6. **A detailed comparison of PL emissions at different spatial positions in pressurized MoSe₂ samples. a**, The PL spectra at the "line-shaped area" (red) and the "normal area" (blue) at 0 GPa. The insets highlight the region of "line-shaped area" and the "normal area". **b**, The PL spectra at the "line-shaped area" (red) and the "normal area" (blue) at 2.2 GPa. **c**, Exciton emission energy of monolayer MoSe₂ as a function of pressure. The red and blue squares represent data obtained from "line-shaped area" and "normal area". **d**, Exciton PL intensity of monolayer MoSe₂ as a function of pressure. The red and blue squares represent data obtained from "line-shaped area" and "normal area". **e**, The PL intensity ratio between "normal area" and "line-shaped area" as a function of pressure.

V. Pressure-dependent band structure calculations in monolayer MoSe$_2$

To understand the blueshift of exciton and trion states with increasing pressure, we performed DFT calculations to obtain the pressure-dependent electronic structures of monolayer MoSe$_2$. These calculated results within the GGA-PBE functional are shown in Supplementary Fig. 7a. We found that the GGA-PBE functional could correctly describe the Λ–K crossover of the conduction band edge with increasing pressure, but underestimated the direct bandgap at the K point. Therefore, we applied the HSE06 functional to correct the bandgap of monolayer MoSe$_2$, as shown in Supplementary Fig. 7b. We found that the HSE06 functional corrected the bandgap at the K point as 1.99 eV for unstrained monolayer MoSe$_2$, which is close to the result (2.08 eV) from G_0W_0 calculations [13]. However, even for unstrained monolayer MoSe$_2$, the conduction band edge is at the Λ point, which is inconsistent with our experimental observations. Thus, the HSE06 functional failed to describe the Λ–K crossover of the conduction band edge with increasing pressure.

To avoid such inconsistency, as shown in Supplementary Fig. 8, we used the direct bandgap of the unstrained monolayer MoSe$_2$ obtained from HSE06 calculations, but the change in the direct bandgap with increasing pressure was calculated by using the GGA-PBE functional. As the pressure increases from 0 to 6.0 GPa, the bandgap increases linearly from 1.99 to 2.16 eV with a slope equal to 28 meV/GPa. The increase in the bandgap directly leads to a blueshift of the exciton and trion emission energies in the PL measurements. Note that the K valley of the conduction band in monolayer MoSe$_2$ moves upward with increasing pressure, whereas the Λ valley moves downward. As a direct result, the conduction band minimum switches from the K valley to the Λ valley (Supplementary Fig. 7a). This result directly demonstrates the Λ–K crossover in our pressurized monolayer MoSe$_2$.

To confirm that our DFT calculation results can describe the real band structure change of the monolayer TMDCs sample under pressure, we systematically compare our calculation results under hydrostatic pressure and the results from previous theoretical report of MoS$_2$ samples under out-of-plane uniaxial pressure [37]. Generally, when the sample undergoes out-of-plane uniaxial pressure, the K valley moves downward with increasing pressure, whereas the Λ valley remains almost unchanged. As a result, the sample maintains a direct bandgap transition under pressure with a lower bandgap. This would expect to result in a redshift of exciton emission energy and increase of PL intensities. In sharp contrast, in our experiments, the exciton emission energy shows clear blueshift and the PL intensity decrease with increasing pressure, showing a typical Λ–K crossover at 3.0 GPa. Such a result can only be well-explained by our DFT calculation with sample under hydrostatic pressure.

382
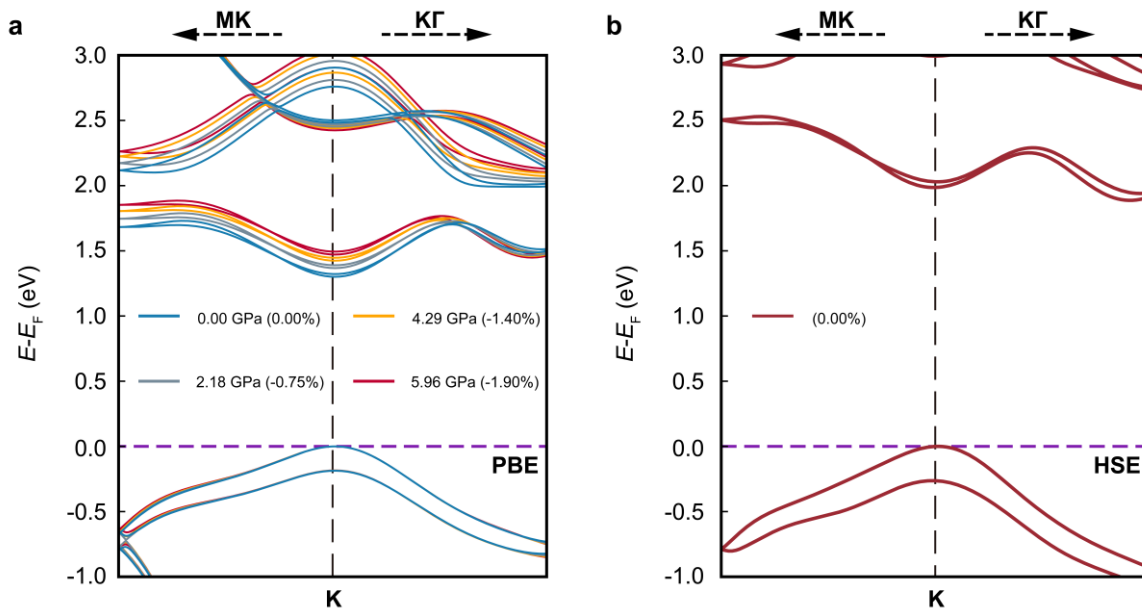
Supplementary Figure 7. a, Calculated band structures of monolayer $MoSe_2$ with the GGA-PBE functional under different pressures in the 0.0 ~ 6.0 GPa range. The zero in the energy axis is set at the Fermi level, as shown by the purple dashed line. The pressure is calculated within the GGA-PBE functional. **b**, The calculated band structures of unstrained monolayer $MoSe_2$ with the HSE06 functional. The zero in the energy axis is set at the Fermi level, as shown by the purple dashed line.


388
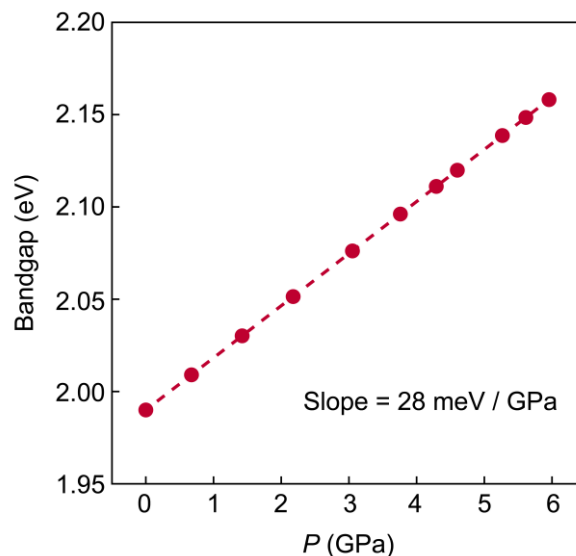
Supplementary Figure 8. The change in bandgap as a function of pressure obtained from DFT calculations. The HSE06 functional is used to obtain the bandgap of the unstrained monolayer $MoSe_2$ and bandgap changes with increasing pressure are obtained from GGA-PBE functionals. The red dashed line is a linear fitting of data with a slope equals to 28 meV/GPa.

To further clarify how pressure modulate the band structures of monolayer $MoSe_2$, we performed DFT to calculate the lattice structures and electronic structures for $MoSe_2$ with and without pressure. As shown in Supplementary Fig. 9b,e, the valence band maximum at Γ point (VBM-Γ) and the conduction band minimum at the K point (CBM-K) in $MoSe_2$ are mainly contributed by the d_{z^2}

15

397   orbital of Mo atoms and p_x/p_y orbitals of Se atoms. Meanwhile, the valence band maximum at K

398   point (VBM-K) and the conduction band minimum at Λ point (CBM-Λ) are dominated by the d_{xy}

399   and $d_{x^2-y^2}$ orbitals of Mo atoms and p_x/p_y orbitals of Se atoms. The energy positions of these states

400   around the Fermi level are determined by the couplings between d orbitals of Mo atoms and p orbitals

401   of Se atoms, which are sensitive to the bond angle and the distances between Mo and Se atoms.

402   With increasing pressure, the bond angle ($\theta = \angle_{\mathrm{Se-Mo-Se}}$ as shown in Supplementary Fig. 9a) and

403   the distance between Se and Se atoms increase, while the distance between Se and Mo atoms

404   decreases (Supplementary Fig. 9c-d). As a result, the overlap between d_{z^2} orbital (Mo) and p_x/p_y

405   orbitals (Se) becomes larger while the overlap between $d_{xy}/d_{x^2-y^2}$ orbitals (Mo) and p orbitals (Se)

406   becomes smaller. Correspondingly, the energy splitting between the VBM-Γ and CBM-K becomes

407   larger while that between the VBM-K and CBM-Λ becomes smaller, which causes the increase of

408   the band gap at the K point and the related Λ-K crossover for conduction bands. Our calculated results

409   are consistent with previous discussions for pressured MoS_2 [38, 39].

410
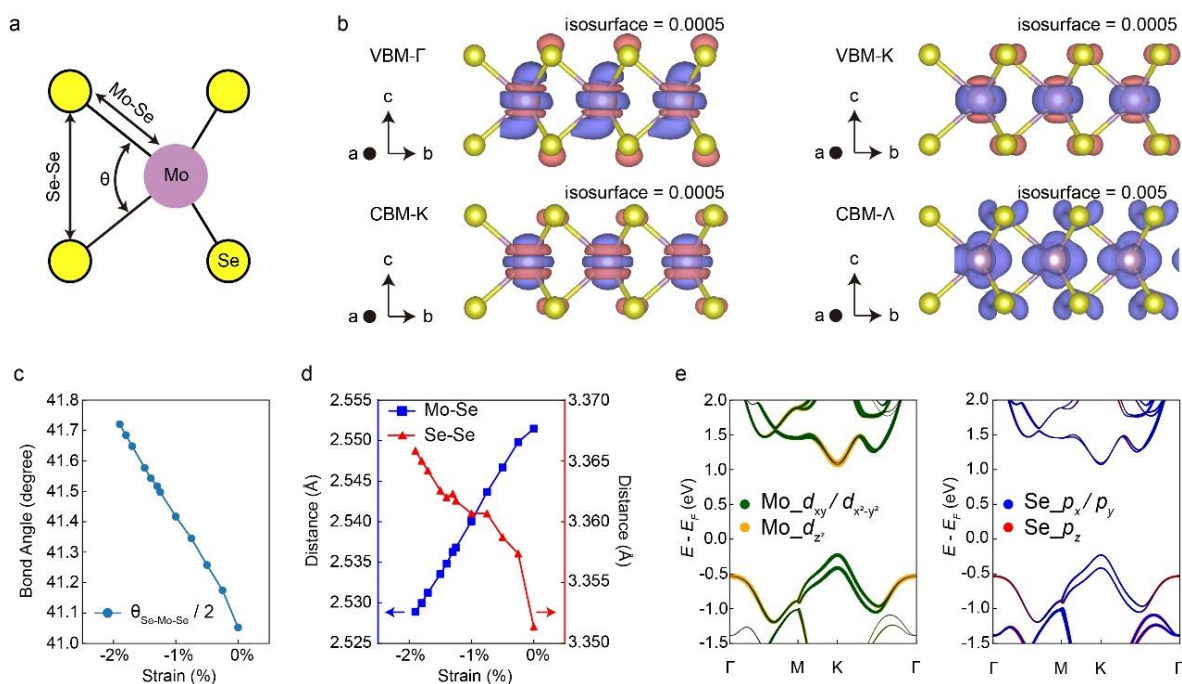
411

412   **Supplementary Figure 9. Illustration of the Λ-K crossover of conduction bands**. **a**, The illustration of the

413   structure of the $MoSe_2$ monolayer. **b**, The visualization of the partial charge density at VBM-Γ, VBM-K, CBM-

414   K, and CBM-Λ for monolayer $MoSe_2$. The Software, VESTA, is used for visualization [40]. **c-d**, The illustration

415   of the variation of the bond angle and the distances between specified atoms along with the applied compressive

416   pressure. **e**, The band structure of the unstrained $MoSe_2$ monolayer.

417

VI. Gate-dependent PL spectra of *h*BN-gated monolayer MoSe₂ devices at various pressures

As mentioned in Fig. 2 in the main text, by applying gate bias (V_G) to change the concentration of electrons, we can control the dominant exciton species (exciton or trion) in MoSe₂ under pressure. Here, in Supplementary Fig. 10a, we show more details of the gate-dependent PL spectra of monolayer MoSe₂ at various pressures from 0.2 GPa to 3.3 GPa. Supplementary Figure 10b shows that the FWHM of the exciton and trion peaks increase with pressures from 0.2 GPa to 3.3 GPa. The reason for the increased FWHM is the pressure-induced indirect band-gap optical transition in the band structure of monolayer MoSe₂. As mentioned in Fig. 1 of the main text, there are two types of excitons corresponding to the direct and indirect bandgap transitions in monolayer MoSe₂ under pressure, in which the direct bandgap transition does not need to involve phonons, while the indirect bandgap transition needs to involve phonons. And the PL emission of monolayer MoSe₂ will contain both direct and indirect excitons at higher pressures. With increasing pressure, the ratio between these two types of excitons changes, and the excitons corresponding to the indirect bandgap transition become dominant with more phonons being involved in the optical transition process. As a result, one can observe the broadening of the PL spectra. Note that the non-hydrostatic component of the pressure at low temperature in our case and its contribution for PL broadening are very small. Specifically, it has been confirmed that the linewidth of the ruby peaks at low temperatures changes little with pressure below 5 GPa, which means even at low temperature the sample should undergo quite good hydrostatic pressure [41]. Therefore, we believe the peak broadening under pressures mainly originates from the emergence of a direct-indirect bandgap transition (the so-called Λ–K crossover).

Note that the exciton and trion emission energies increase slowly with pressure below 2.0 GPa and start to quickly increase with a sudden change in exciton and trion emission energy under the pressure over 2.0 GPa (details in Fig. 3b in main text). Such behavior is slightly different from the theoretical prediction, where the exciton and trion emission energies increase linearly with increasing pressure. We believe the reason for the sudden change in exciton and trion emission energy is that, below 2.0 GPa, the pressure in the sample at 77 K is partially released with temperature cooling while the pressure is estimated by ruby PL spectra at 300 K. Specifically, when the pressure is determined at room temperature and the DAC is cooled to 77 K, the pressure usually changes somewhat due to the thermal contraction of the DAC, etc. The difference in the pressure values at room and low temperatures is rather nonmonotonic and unpredictable, which results in the uncertainty in the nominal pressure values. As a result, one may observe that the exciton/trion energy changes slowly with pressure below 2.0 GPa and starts to change quickly above 2.0 GPa. Fortunately, both the experiments and theoretical prediction yield a total blueshift of ~55 meV in exciton and trion emission energy from 0 to 2.3 GPa. Therefore, the sudden jump will not influence our conclusion that exciton and trion emission energies show dramatic blueshift with increasing pressure and will not affect the estimation of trion binding energy values under different pressures.

455
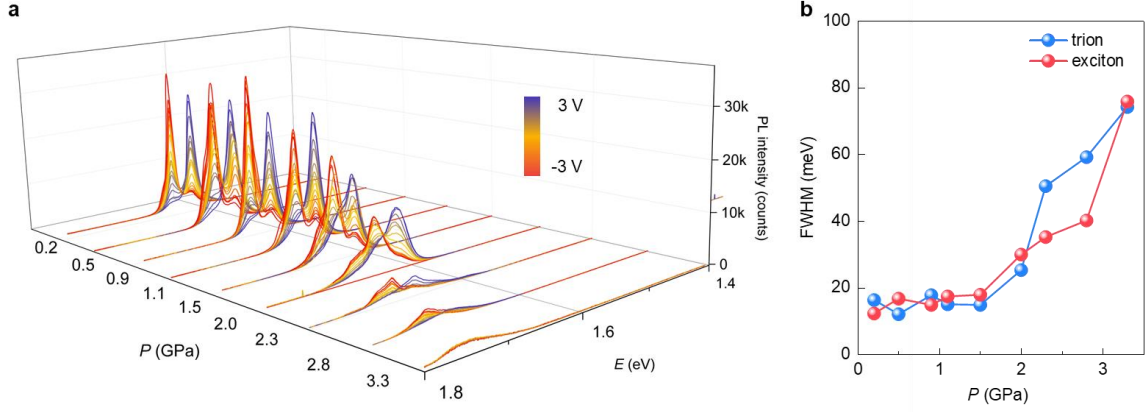
Supplementary Figure 10. Gate-dependent PL spectra at various pressures. **a**, Gate-dependent PL spectra
at various pressures. The data are obtained at a fixed temperature of 77 K at 0.2, 0.5, 0.9, 1.1, 1.5, 2.0, 2.3, 2.8
and 3.3 GPa. The gate bias is applied from −3 V (red curve) to 3 V (blue curve). The PL spectra obtained at
different pressures are shifted for better visualization. **b**, Full width at half maximum (FWHM) of the exciton
(red balls) and trion (blue balls) peaks as a function of pressure.

To understand the exciton-to-trion transition under pressure, we present the colored mapping for the
sum of the integrated area of trion and exciton PL peaks ($I_{\text{total}} = I_{\text{trion}} + I_{\text{exciton}}$) and the color
mapping for the weight of the integrated area of the trion PL peak (denoted as $I_{\text{trion}}/I_{\text{total}}$) in Fig.
2i,j in the main text. Here, in Supplementary Fig. 11, we show all the original data of excitons, trions,
and their total integrated area of PL peaks as a function of V_G at various pressures. One can see that
the I_{total} values change slightly before 2.0 GPa and start to drop quickly with increasing pressure
after 2.0 GPa and eventually decrease to a very low level at 3.3 GPa, which directly corresponds to
the Λ–K crossover with increasing pressure. Such pressure-dependent PL emission intensities can be
understood as follows: first, for pressures below 2.0 GPa, all the PL emissions come from the direct
K–K transition and therefore change little with increasing pressure; second, for pressures from 2.0 to
2.8 GPa, the indirect Λ–K transition starts to be involved; therefore, the PL emissions drop quickly
in this pressure regime. Third, for pressures above 2.8 GPa, all the PL emissions come from the
indirect Λ–K transition, so the total PL emission intensities decrease to a very low level. Notably,
the gate-controlled exciton-to-trion transition can be realized in monolayer MoSe₂ below 2.8 GPa,
while no apparent gate response of PL emissions is observed at 3.3 GPa (Supplementary Fig. 10a).
This result directly confirms that the sample has completely changed to an indirect bandgap
semiconductor after 2.8 GPa; hence the exciton and trion from the direct transition are no longer
observed.

We also estimate the two-dimensional carrier density (n_{2D}) in monolayer MoSe₂ in the above gating
process, by considering the Au/h-BN/MoSe₂ sandwiched device as a parallel plate capacitor. The
amount of charge per unit area can be written as:

$$en_{2D} = \varepsilon_0 \varepsilon_r / d \times (V_G - V_{\text{th}})$$

where e is the electron charge, ε_0 is the vacuum permittivity, $d = 20$ nm and $\varepsilon_r = 4$ are the thickness
and the relative dielectric constant of h-BN, respectively, and $V_{\text{th}} \approx -2$ V is the threshold voltage that

485 corresponds to the charge neutrality point of the sample (Supplementary Fig. 11a). Based on the
486 above equation, we actually modulate the monolayer MoSe$_2$ sample from near neutrality to an
487 electron density of approximately 5 ($\pm$1) $\times$ 10^{12} cm^{-2} when increasing V_G from $-$3 to 3 V.

488 In the pressure-dependent PL spectra of monolayer MoSe$_2$, one can see a shoulder on the higher
489 energy side of the exciton peak for PL spectra at higher pressures (Supplementary Fig. 12). This
490 higher energy peak might result from the newly-generated defect states under pressure in monolayer
491 MoSe$_2$, as shown in Supplementary Fig. 12c. For example, it has been reported recently that defects
492 in MoSe$_2$ such as Se atom vacancies can generate defect states in the energy gap [42-45]. The energy
493 level of these defects can be either higher or lower than the exciton energy. These defect states with
494 higher energy may appear under pressure and can show blueshift with increasing pressure due to the
495 direct bandgap increasing, which is consistent with the blueshift of the higher energy peak with
496 pressure in our experiment. Since the focus of this paper is to demonstrate the robust trion binding
497 energy, which is only related to the exciton and trion emission energy under pressure, we believe the
498 shoulder on the higher energy side of the exciton peak would not affect our conclusions. The study
499 of this higher energy peak under pressure can be an interesting research topic in near future.
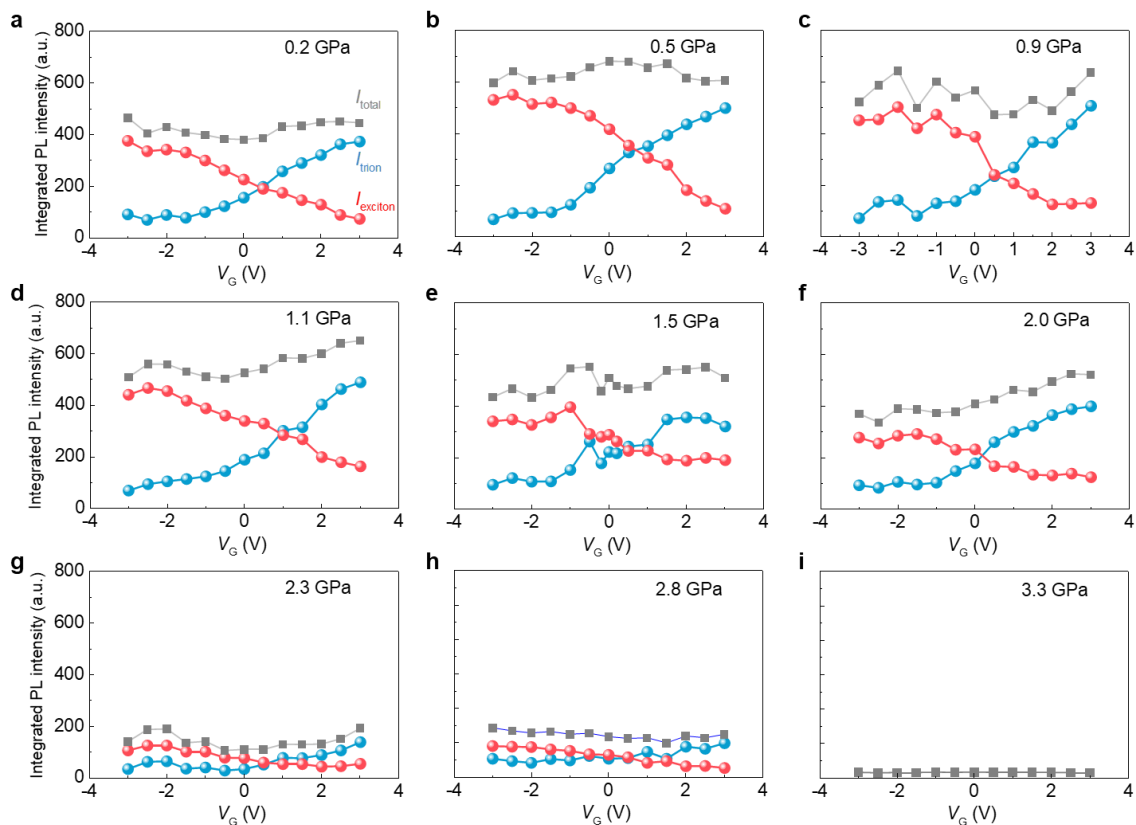
501 **Supplementary Figure 11. Gate-tuned exciton-trion transition under various pressures. a-i,** Exciton (red
502 balls), trion (blue balls), and total (gray squares) integrated PL intensities as functions of V_G at different
503 pressures. Note that at 3.3 GPa, the gate-controllable exciton-to-trion transition is not observed because the
504 sample changes from a direct bandgap to an indirect bandgap, and all the PL emissions come from the indirect
505 transition. The integrated PL intensities are obtained by fitting the PL spectra with multiple Voigt functions.
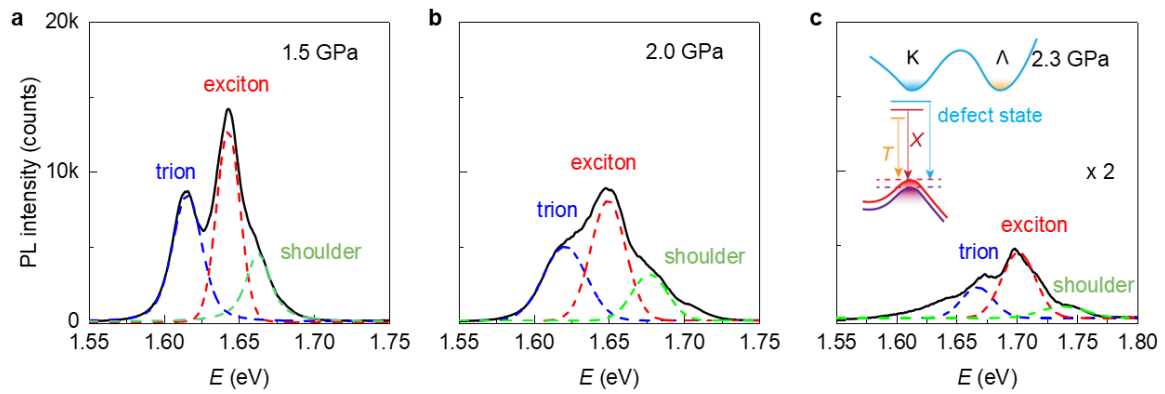
Supplementary Figure 12. Origin of the higher energy peak in monolayer MoSe$_2$ under pressure. **a-c**, PL spectra of monolayer MoSe$_2$ at zero gate bias under 1.5 GPa (a), 2.0 GPa (b), and 2.3 GPa (c). The red and orange dashed curves represent the fitting of the exciton and trion peaks. The green dashed curves represent the fitting of the higher energy peak. Inset: Schematics of the band structure of monolayer MoSe$_2$ under pressure. The red and orange arrows represent the recombination of excitons and trions. The blue arrows represent the recombination of a higher energy defect state.

VII. Precise determination of the exciton and trion emission energy under pressure using
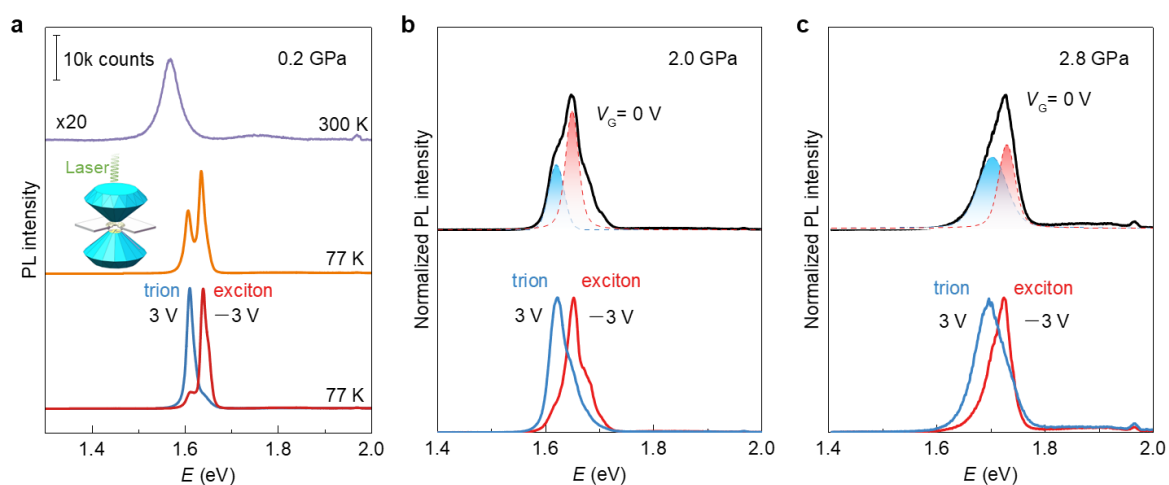*gating-under-pressure* **technique**

To highlight the reversibility of the gate-tuned exciton-trion transition in pressurized monolayer $MoSe_2$, we provide the PL intensities of excitons and trions at gate sweep cycles ranging from −3 V to 3 V in Supplementary Fig. 13. Both the PL intensities of the exciton and trion almost return to their initial values after the gate-sweeping loop, indicating that the process is reversible in the bias range of −3 V to 3 V. Furthermore, such a reversible gating process is independent of the external pressure, as shown in Supplementary Fig. 13b,d (0.2 and 0.9 GPa, respectively). Note that the PL intensity as a function of V_G exhibits a small hysteresis, which is quite common in those cases in *h*-BN or EDL gate devices [46].
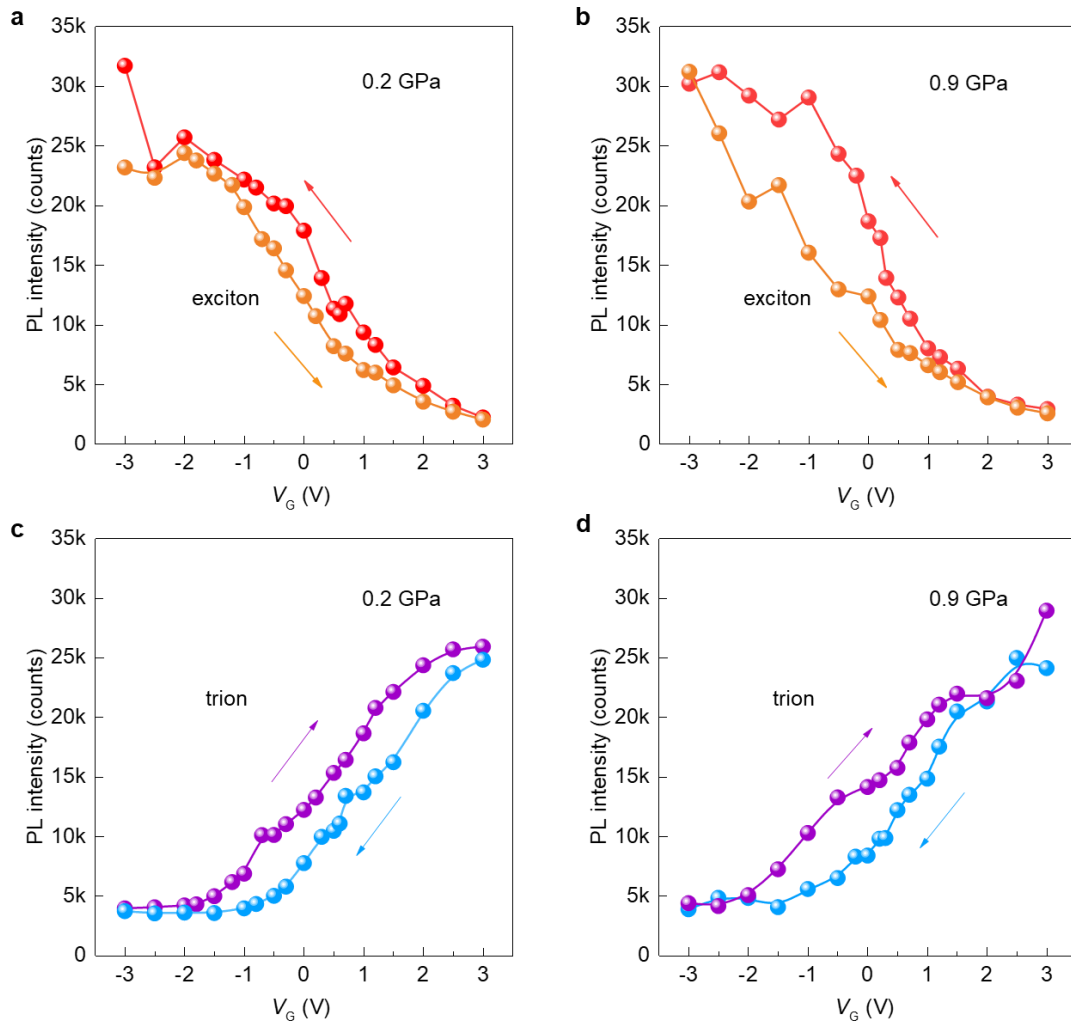
Supplementary Figure 13. Reversible gate-tuned exciton-trion transition under pressure. PL intensity of exciton as a function of gate bias, obtained at **a**, 0.2 GPa and **b**, 0.9 GPa. The orange (or red) balls represent data obtained by applying V_G from –3 V to 3 V (3 V to –3 V). PL intensity of trion as a function of gate bias, obtained at **c**, 0.2 GPa and **d**, 0.9 GPa. The purple (or blue) balls represent data obtained by applying V_G from –3 V to 3 V (3 V to –3 V). The data are obtained at 77 K.

To highlight the technical advance of our *gating-under-pressure* technique at low temperature for simultaneously observing excitons and trions under pressure, we compare the PL spectra of

monolayer MoSe$_2$ at 300 K, 77 K, and 77 K with gating. As shown in Supplementary Fig. 14a, after lowering the temperature to 77 K, the FWHM of the exciton peak becomes relatively narrow (from 51 meV to 12 meV), and the PL intensity is magnified over 20 times larger than its original value at 300 K. More importantly, as shown in the bottom panel in Supplementary Fig. 14a, by applying a ±3.0 V back gate voltage (V_G) to electrically tune the electron concentration in MoSe$_2$, exciton and trion emission peaks can be distinguished in the spectra and switched between exciton-dominated and trion-dominated states. Such electrical control of exciton and trion states is vital to studying excitonic physics under pressure. As shown in Supplementary Fig. 14b,c, at 2.0 GPa or 2.8 GPa, it is difficult to distinguish excitons and trions at $V_G = 0$ V due to the peak broadening induced by pressure, and a tricky fitting of PL spectra is required to obtain the exciton and trion emission energies. However, since we have demonstrated that our fully reversible gate process (Supplementary Fig. 13) could dramatically tune the PL intensity of excitons and trions without changing their emission energy (Fig. 3a in the main text), we can directly determine the emission energy of excitons (or trions) by analyzing the PL spectra at $V_G = -3$ V (or 3 V), as shown in Supplementary Fig. 14b,c. Therefore, by applying electrical gating within DAC at low temperature, our *gating-under-pressure* technique provides opportunities to study excitonic behavior and many-body effects under pressure. To the best of our knowledge, this work is the first demonstration of gate-controlled trion (and exciton) states in monolayer TMDCs under high pressure via a gating-under-pressure technique (Table S1), which can indeed effectively tune the band structure of TMDCs and the trion (and exciton) states therein.

Supplementary Figure 14. *Gate-under-pressure* **technique for exciton and trion states of monolayer MoSe$_2$ determination under pressure. a**, A direct comparison of the PL spectra of monolayer MoSe$_2$ obtained at 300 K (purple curve), 77 K (orange curve), and 77 K with a back gate bias of ±3 V (red and blue curves). The PL spectra obtained at 300 K are magnified 20 times. All the PL spectra are shifted on the Y-axis for better visualization. The inset is a schematic figure for high-pressure DAC setup. A direct comparison of the PL spectra of monolayer MoSe$_2$ with and without a gate at 2.0 GPa, **b**, or 2.8 GPa, **c**. The red, black, blue plots represent the PL spectra obtained at $V_G = -3, 0, 3$ V. The PL spectra at $V_G = 0$ V are shifted on the Y-axis for better visualization. The red and blue dashed plots are fitting results for exciton and trion peaks by the multiple Voigt functions. All PL spectra were obtained at 77 K.

Table S1: A summary of the study of pressurized monolayer TMDCs

Material	Theoretical		Experimental				Refs.
	Methods	Results	Methods	E_{exciton}	E_{trion}	Temperature	
MoSe₂	**DFT, QMC**	$\boldsymbol{E_g}$ $\boldsymbol{E_{\text{exciton}}}$ $\boldsymbol{E_{\text{trion}}}$	**Gated PL**	**Yes**	**Yes**	**300 K** **77 K**	**This work**
MoS₂	DFT	E_g	NA	Yes	NA	NA	[38]
MoS₂	DFT	E_g	NA	Yes	NA	NA	[47]
MoS₂	DFT	E_g	PL no gate	Yes	NA	300 K	[48]
MoS₂	DFT	E_g	PL no gate	Yes	NA	300 K	[39]
MoS₂	DFT	E_g	PL no gate	Yes	NA	300 K	[49]
MoS₂, MoSe₂, WS₂, WSe₂	DFT	E_g	Reflectance no gate	Yes	NA	300 K	[50]
WSe₂	DFT	E_g	PL no gate	Yes	NA	300 K	[51]
MoSe₂	DFT	E_g	PL no gate	Yes	NA	300 K	[52]
MoSe₂	DFT	E_g	PL no gate	Yes	NA	300 K	[53]

562 NA: not applicable.

References:

[1] A. Mujica, A. Rubio, A. Muñoz, R.J. Needs, High-pressure phases of group-IV, III–V, and II–VI compounds. *Rev. Mod. Phys.* **75**, 863–912 (2003).

[2] G. Kresse, J. Furthmüller, Efficient iterative schemes for *ab initio* total-energy calculations using a plane-wave basis set. *Phys. Rev. B* **54**, 11169–11186 (1996).

[3] P.E. Blöchl, Projector augmented-wave method. *Phys. Rev. B* **50**, 17953–17979 (1994).

[4] G. Kresse, D. Joubert, From ultrasoft pseudopotentials to the projector augmented-wave method. *Phys. Rev. B* **59**, 1758–1775 (1999).

[5] J.P. Perdew, K. Burke, M. Ernzerhof, Generalized gradient approximation made simple. *Phys. Rev. Lett.* **77**, 3865–3868 (1996).

[6] J. Klimeš, D.R. Bowler, A. Michaelides, Chemical accuracy for the van der Waals density functional. *J. Phys.: Condens. Matter* **22**, 022201 (2010).

[7] J. Klimeš, D.R. Bowler, A. Michaelides, Van der Waals density functionals applied to solids. *Phys. Rev. B* **83**, 195131 (2011).

[8] S. Horzum, H. Sahin, S. Cahangirov, P. Cudazzo, A. Rubio, T. Serin, F.M. Peeters, Phonon softening and direct to indirect band gap crossover in strained single-layer $MoSe_2$. *Phys. Rev. B* **87**, 125415 (2013).

[9] S. Kumar, U. Schwingenschlögl, Thermoelectric response of bulk and monolayer $MoSe_2$ and WSe_2. *Chem. Mater.* **27**, 1278-1284 (2015).

[10] J. Xia, J. Yan, Z. Wang, Y. He, Y. Gong, W. Chen, T.C. Sum, Z. Liu, P.M. Ajayan, Z. Shen, Strong coupling and pressure engineering in WSe_2–$MoSe_2$ heterobilayers. *Nat. Phys.* **17**, 92–98 (2020).

[11] J. Heyd, G.E. Scuseria, M. Ernzerhof, Hybrid functionals based on a screened Coulomb potential. *J. Chem. Phys.* **118**, 8207–8215 (2003).

[12] J. Heyd, G.E. Scuseria, M. Ernzerhof, Erratum: "Hybrid functionals based on a screened Coulomb potential" [*J. Chem. Phys.* **118**, 8207 (2003)]. *J. Chem. Phys.* **124**, 219906 (2006).

[13] H.-g. Kim, H.J. Choi, Thickness dependence of work function, ionization energy, and electron affinity of Mo and W dichalcogenides from DFT and GW calculations. *Phys. Rev. B* **103**, 085404 (2021).

[14] T.C. Berkelbach, M.S. Hybertsen, D.R. Reichman, Theory of neutral and charged excitons in monolayer transition metal dichalcogenides. *Phys. Rev. B* **88**, 045318 (2013).

[15] E. Courtade *et al.*, Charged excitons in monolayer WSe_2: Experiment and theory. *Phys. Rev. B* **96**, 085302 (2017).

[16] C. Fey, P. Schmelcher, A. Imamoglu, R. Schmidt, Theory of exciton-electron scattering in atomically thin semiconductors. *Phys. Rev. B* **101**, 195417 (2020).

[17] N.S. Rytova, The screened potential of a point charge in a thin film. *Moscow University Physics Bulletin* **3**, 18 (1967).

[18] L.V. Keldysh, Coulomb interaction in thin semiconductor and semimetal films. *Sov. J. Exp. Teor. Phys. Lett.* **29**, 658 (1979).

[19] P. Cudazzo, C. Attaccalite, I.V. Tokatly, A. Rubio, Strong charge-transfer excitonic effects and the Bose-Einstein exciton condensate in graphene. *Phys. Rev. Lett.* **104**, 226804 (2010).

[20] P. Cudazzo, I.V. Tokatly, A. Rubio, Dielectric screening in two-dimensional insulators: Implications for excitonic and impurity states in graphene. *Phys. Rev. B* **84**, 085406 (2011).

[21] D.S. Hughes, C. Eckart, The effect of the motion of the nucleus on the spectra of Li I and Li II. *Phys. Rev.* **36**, 694–698 (1930).

[22] G. L. Doll, in *Handbook of Optical Constants of Solids,* E. D. Palik, Ed. (Academic Press, Burlington,

606   1997), pp. 425–443.

[23] K.F. Mak, K. He, C. Lee, G.H. Lee, J. Hone, T.F. Heinz, J. Shan, Tightly bound trions in monolayer MoS$_2$, *Nat. Mater.* **12**, 207–211 (2013).

[24] J.S. Ross, S. Wu, H. Yu, N.J. Ghimire, A.M. Jones, G. Aivazian, J. Yan, D.G. Mandrus, D. Xiao, W. Yao, X. Xu, Electrical control of neutral and charged excitons in a monolayer semiconductor, *Nat. Commun.* **4**, 1474 (2013).

[25] G. Wang *et al*, Colloquium: Excitons in atomically thin transition metal dichalcogenides, *Rev. Mod. Phys.* **90**, 021001 (2018).

[26] M.M. Ugeda *et al*, Giant bandgap renormalization and excitonic effects in a monolayer transition metal dichalcogenide semiconductor, *Nat. Mater.* **13**, 1091–1095 (2014).

[27] A. Raja *et al*, Coulomb engineering of the bandgap and excitons in two-dimensional materials, *Nat. Commun.* 8, 15251 (2017).

[28] F. Liu, M.E. Ziffer, K.R. Hansen, J. Wang, X. Zhu, Direct Determination of Band-Gap Renormalization in the Photoexcited Monolayer MoS$_2$, *Phys. Rev. Lett.* **122**, 246803 (2019).

[29] Y. Lee *et al.*, Boosting quantum yields in two-dimensional semiconductors via proximal metal plates. *Nat. Commun.* **12**, 7095 (2021).

[30] C. Lee, H. Yan, L.E. Brus, T.F. Heinz, J. Hone, S. Ryu, Anomalous lattice vibrations of single- and few-Layer MoS$_2$. *ACS Nano* **4**, 2695–2700 (2010).

[31] A.G. Bagnall, W.Y. Liang, E.A. Marseglia, B. Welber, Raman studies of MoS$_2$ at high pressure. *Physica B+C* **99**, 343–346 (1980).

[32] M. Yang, X. Cheng, Y. Li, Y. Ren, M. Liu, Z. Qi, Anharmonicity of monolayer MoS$_2$, MoSe$_2$, and WSe$_2$: A Raman study under high pressure and elevated temperature, *Appl. Phys. Lett.* 110 093198 (2017).

[33] L.G. Pimenta Martins *et al.*, Pressure tuning of minibands in MoS$_2$/WSe$_2$ heterostructures revealed by moiré phonons, *Nat. Nanotechnol.* (2023) https://doi.org/10.1038/s41565-023-01413-3.

[34] H. Li, A.W. Contryman, X. Qian, S.M. Ardakani, Y. Gong, X. Wang, J.M. Weisse, C.H. Lee, J. Zhao, P.M. Ajayan, J. Li, H.C. Manoharan, X. Zheng, Optoelectronic crystal of artificial atoms in strain-textured molybdenum disulphide, *Nat. Commun.*, **6**, 7381 (2015)

[35] H.J. Conley, B. Wang, J.I. Ziegler, R.F. Haglund, Jr., S.T. Pantelides, K.I. Bolotin, Bandgap engineering of strained monolayer and bilayer MoS$_2$. *Nano Lett.* **13**, 3626–3630 (2013).

[36] Y. Wang, C. Cong, C. Qiu, T. Yu, Raman spectroscopy study of lattice vibration and crystallographic orientation of monolayer MoS$_2$ under uniaxial strain. *Small* **9**, 2857–2861 (2013).

[37] H. Yuan *et al.*, Evolution of the valley position in bulk transition-metal chalcogenides and their monolayer limit, *Nano Lett.* **16**, 4738–4745 (2016).

[38] X. Fan, C.H. Chang, W.T. Zheng, J.-L. Kuo, D.J. Singh, The Electronic Properties of Single-Layer and Multilayer MoS$_2$ under High Pressure, *J. Phys. Chem. C*, **119** 10189-10196 (2015).

[39] L. Fu, Y. Wan, N. Tang, Y.-m. Ding, J. Gao, J. Yu, H. Guan, K. Zhang, W. Wang, C. Zhang, J.-j. Shi, X. Wu, S.-F. Shi, W. Ge, L. Dai, B. Shen, K–Λ crossover transition in the conduction band of monolayer MoS$_2$ under hydrostatic pressure, *Sci. Adv.* **3**, e1700162 (2017).

[40] K. Momma, F. Izumi, VESTA 3 for three-dimensional visualization of crystal, volumetric and morphology data, *J. Appl. Crystallogr.* **44**, 1272–1276 (2011).

[41] N. Tateiwa, Y. Haga, Evaluations of pressure-transmitting media for cryogenic experiments with diamond anvil cell, *Rev. Sci. Instrum*, **80** 123901 (2009).

[42] S. Refaely-Abramson, D.Y. Qiu, S.G. Louie, J.B. Neaton, Defect-Induced Modification of Low-Lying Excitons and Valley Selectivity in Monolayer Transition Metal Dichalcogenides, *Phys. Rev. Lett.* **121**

650   167402 (2018).

651 [43] T.Y. Jeong, H. Kim, S.J. Choi, K. Watanabe, T. Taniguchi, K.J. Yee, Y.S. Kim, S. Jung, Spectroscopic
652   studies of atomic defects and bandgap renormalization in semiconducting monolayer transition metal
653   dichalcogenides, *Nat. Commun.* **10**, 3825 (2019).

654 [44] K. Greben, S. Arora, M.G. Harats, K.I. Bolotin, Intrinsic and Extrinsic Defect-Related Excitons in
655   TMDCs, *Nano Lett.* **20**, 2544–2550 (2020).

656 [45] P. Vancso, G.Z. Magda, J. Peto, J.Y. Noh, Y.S. Kim, C. Hwang, L.P. Biro, L. Tapaszto, The intrinsic
657   defect structure of exfoliated MoS_2 single layers revealed by Scanning Tunneling Microscopy, *Sci. Rep.*
658   **6**, 29726 (2016).

659 [46] C. Lee, S. Rathi, M.A. Khan, D. Lim, Y. Kim, S.J. Yun, D.-H. Youn, K. Watanabe, T. Taniguchi, G.-H.
660   Kim, Comparison of trapped charges and hysteresis behavior in *h*BN encapsulated single MoS_2 flake
661   based field effect transistors on SiO_2 and *h*BN substrates, *Nanotechnol.* **29,** 335202 (2018).

662 [47] H. Peelaers, C.G. Van de Walle, Elastic Constants and Pressure-Induced Effects in MoS_2, *J. Phys. Chem.*
663   *C* **118**, 12073–12076 (2014).

664 [48] X. Dou, K. Ding, D. Jiang, B. Sun, Tuning and Identification of Interband Transitions in Monolayer and
665   Bilayer Molybdenum Disulfide Using Hydrostatic Pressure, *ACS Nano* **8**, 7458–7464 (2014).

666 [49] A.P. Nayak, T. Pandey, D. Voiry, J. Liu, S.T. Moran, A. Sharma, C. Tan, C.H. Chen, L.J. Li, M.
667   Chhowalla, J.F. Lin, A.K. Singh, D. Akinwande, Pressure-dependent optical and vibrational properties of
668   monolayer molybdenum disulfide, *Nano Lett.* **15**, 346–353 (2015).

669 [50] F. Dybala, M.P. Polak, J. Kopaczek, P. Scharoch, K. Wu, S. Tongay, R. Kudrawiec, Pressure coefficients
670   for direct optical transitions in MoS_2, $MoSe_2$, WS_2, and WSe_2 crystals and semiconductor to metal
671   transitions, *Sci. Rep*. **6**, 26663 (2016).

672 [51] Y. Ye, X. Dou, K. Ding, D. Jiang, F. Yang, B. Sun, Pressure-induced K–Λ crossing in monolayer WSe_2,
673   *Nanoscale* **8**, 10843–10848 (2016).

674 [52] X. Fu, F. Li, J.F. Lin, Y. Gong, X. Huang, Y. Huang, B. Han, Q. Zhou, T. Cui, Pressure-Dependent Light
675   Emission of Charged and Neutral Excitons in Monolayer $MoSe_2$, *J. Phys. Chem. Lett.* **8**, 3556–3563
676   (2017).

677 [53] X. Cheng, L. Jiang, Y. Li, H. Zhang, C. Hu, S. Xie, M. Liu, Z. Qi, Using strain to alter the energy bands
678   of the monolayer $MoSe_2$: A systematic study covering both tensile and compressive states, *Appl. Surf. Sci.*
679   **521**, 146398 (2020).

680

681

682